Finite-Wavelength Instabilities of a Coupled Density Front

NATHAN PALDOR* AND MICHAEL GHIL**

Department of Atmospheric Sciences, University of California, Los Angeles, California

(Manuscript received 5 December 1988, in final form 11 August 1989)

ABSTRACT

Finite-wavelength instabilities of a coupled density front with zero potential vorticity are found for the single-layer and the two-layer problems. These instabilities result from the resonance between two distinct waves whose real phase speeds coalesce. In the single-layer problem, the range of wavenumbers over which this coalescence takes place decreases with increasing wavenumber; consequently, the instability exponents and the growth rates also decrease. For shallow lower layers, the coalescence range increases with increasing wavenumber; at large wavenumbers, the coalescence range becomes continuous, while the instability exponent is approaching a constant value. The growth rate in the two-layer problem increases, therefore, linearly with wavenumber and the short waves grow fastest. These short-wave instabilities are qualitatively reminiscent of small-scale features along coastal fronts and in laboratory experiments.

1. Introduction

Linear instabilities on geostrophic fronts have been studied extensively in recent years. A common simplification is to regard the vertical structure as consisting of two layers, each having uniform density, thus replacing the continuous density variation with depth by a hydrostatic matching condition at the interface separating the two layers. This is a good approximation when a region of fast vertical density variation exists.

In a frontal problem, the interface between the two layers intersects the more-or-less horizontal boundary of the fluid, e.g., the ocean surface or bottom, along the so-called free streamline. Away from the free streamline, the front can either extend to infinity, as in the Gulf Stream, or it can intersect the surface (or the bottom) along a second free streamline. The former case is that of an isolated front, the latter is called a coupled front.

Coupled fronts occur in the northward spreading of Antarctic Bottom Water (AABW) in the South Atlantic (Whitehead and Worthington 1982) and in the Denmark Strait overflow (Smith 1976). A particularly tractable case of coupled front obtains by assuming that the potential vorticity is zero throughout the upper layer. In this case the velocity profile in the upper layer is linear and hence, by geostrophy, the interface depth is quadratic. These assumptions allow a rather complete perturbation analysis to be carried out.

A linear stability analysis for a coupled front with an infinitely-deep lower layer was carried out by Griffiths et al. (1982, GKS hereafter). They found analytically an instability for very small wavenumbers, and extended their study numerically to higher wavenumbers. The GKS instability has a finite wavenumber cutoff, above which no instabilities were found.

In subsequent work, Paldor and Killworth (1987, hereafter PK) studied the two-layer problem encountered when the dynamics of the lower layer is taken into account for arbitrary upper-layer potential vorticity. Using a combined expansion in both small wavenumber and large depth ratio, they found another instability to occur when the lower layer is not very deep. This instability vanishes when the lower layer becomes sufficiently deep. On the other hand, PK showed that the long-wave, GKS instability for a single layer can be extended analytically to the two-layer problem, but vanishes when the lower layer is sufficiently shallow. Paldor and Killworth also extended numerically the two-layer growth rate for both types of long-wave instability to finite wavenumbers. They showed that the computed growth rate fits the experimental data of GKS much better than the single-layer growth rate. The transition between the GKS instability and the two-layer one of PK occurs at a large depth ratio of $O(10^2)$.

Both the GKS and PK approaches yield essentially long-wave instabilities. The GKS experiments, however, indicate that the temporal growth of the instabilities occurs over a wide range of wavenumbers. Much of the growth takes place at short wavelengths, outside the range of applicability of either the GKS or the PK

* Permanent affiliation: Hebrew University of Jerusalem.
** Also Institute of Geophysics and Planetary Physics, UCLA.

Corresponding author address: Prof. Michael Ghil, Dept. of Atmospheric Sciences, UCLA, 405 Hilgard Avenue, Los Angeles, CA 90024-1565.

stability analyses. In this paper we report on short-wave instabilities of both the single-layer and the two-layer fronts, which are not an extension of either the GKS or the PK long-wave instabilities.

These additional instabilities result from a resonance between two distinct waves, whose phase speeds coalesce within a certain wavenumber range. A continuous two-layer instability curve is shown to exist for large wavenumbers, provided the lower layer is sufficiently shallow. This continuous growth-rate curve breaks up into separate instabilities with smaller growth, and eventually vanishes as the lower layer becomes deep enough.

The short-wave instabilities obtained here compete, in a certain depth-ratio range and in the absence of dissipation, with either the GKS or the PK instability. A full theory of the observed instabilities will require the inclusion of nonlinear terms and of dissipation, which will resolve the competition between linear instabilities and lead to an equilibrated, but probably chaotic flow regime (Ghil and Childress 1987; Pedlosky 1987).

A first step in this direction was taken by Paldor (1986), who developed a nonlinear, long-wave theory for the single-layer front and obtained analytically both solitary and standing waves of finite amplitude. The amplitude–wavelength relation of these waves was shown to be comparable with the experimental results of GKS. Paldor's nonlinear evolution equation could, however, not be integrated numerically, because of the ill-posedness of certain terms. Hence the effect of the nonlinear terms on the GKS instability could not be studied in detail. The equilibration of the linear instabilities by dissipation and the nonlinear terms in the two-layer problem is under study.

We treat the single-layer problem in section 2 and two-layer instabilities in section 3. In section 4 we discuss the relevance of the results to observations of oceanic frontal flows and to the GKS experiments, and summarize our findings.

2. Single-layer instabilities

a. Formulation and methodology

The coupled density front of zero potential vorticity is shown in Fig. 1. The complete formulation of the single-layer problem was given in GKS and Paldor (1986). For the reader's convenience, we recapitulate here just the governing equation. The nondimensional eigenvalue equation for the single-layer problem, i.e., $r \to \infty$, in Fig. 1, is

$$(Hu'_y)_y - k^2[H - (U - C)^2]u' = 0, \quad (2.1)$$

with subscripts denoting differentiation. Here $u'(y)$ is the amplitude of the downstream velocity perturbation (into the plane of the paper) having a wavenumber k and phase speed C, $H(y) = -y(y + 1)/2$ is the mean depth of the upper layer and $U(y) = y + \frac{1}{2}$ is its velocity. The two free streamlines are located, in this formulation, at $y = 0$ and $y = -1$. For a complete derivation of this equation see GKS (where the initial scaling is slightly different, so the free streamlines are located at $y = \pm\sqrt{2}$) and Paldor (1986).

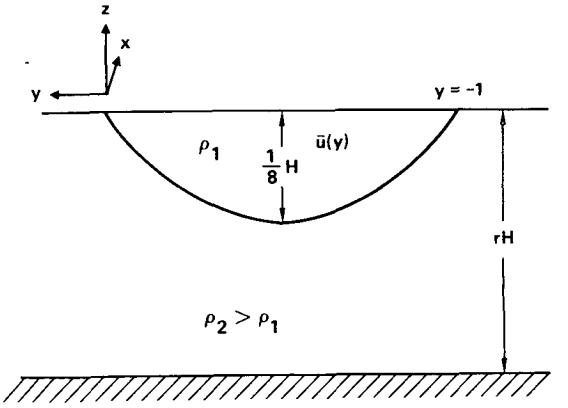

FIG. 1. The coupled front of zero potential vorticity. The interface depth is parabolic and its maximum value is $(1/8)H$, where H is a height scale. The total depth is rH. The lower layer is initially at rest, while the upper layer has an initial downstream velocity U_1 which varies linearly with y. The single-layer problem corresponds to letting r tend to infinity and the pressure in the lower layer approach zero. The Denmark Strait overflow and northward spreading of AABW correspond to an upside-down version of the figure.

As usual, unstable modes are characterized by a complex C and for these modes u' is also complex. The long-wave (GKS) instability is obtained by expanding u' and C in a power series with respect to k; once $\mathrm{Im}(C)$ is found analytically for small enough k it can be easily extended numerically to higher k values. The easiest way to find $\mathrm{Im}(C(k))$ for all k is to increase k, starting from a very small value, and at each k use as initial guess the value of $\mathrm{Im}(C)$ found for the previous k. This procedure works well in a range of k for which the curve $\mathrm{Im}(C)$ versus k is continuous. Beyond the cutoff value of this range there is no good initial guess, and GKS found no instability for moderate or large k.

In order to find finite-wavelength instabilities, one has to employ a numerical procedure that does not necessitate a good initial guess. The procedure we used is the following. First, the eigenvalue equation (2.1) is symmetrized by defining a new independent variable $z = 2y + 1$, so that the free streamlines are located at $z = \pm 1$ and the equation becomes

$$[(1 - z^2)u_z]_z + (k^2/4)(3z^2 - 1 - 8Cz + 8C^2)u = 0, \quad (2.2)$$

where $u(z) = u'(y)$.

Assuming $kC \sim 1$ in the long-wave limit, $k \to 0$, Eq. (2.2) becomes a Legendre equation with real eigenvalues

$$2(kC)^2 = n(n + 1), \quad n = 0, 1, 2, \cdots. \quad (2.3)$$

The $n = 0$ mode violates the condition $kC \sim 1$ and indeed, for $k = 0$, this mode is associated with the GKS instability in Eq. (2.2). All other modes of (2.2) are actually stable, i.e., have C real, when k is sufficiently small.

To find finite-wavelength instabilities, we have to solve Eq. (2.2) for arbitrary k and determine those k-values for which C becomes complex. To achieve this, we expand (2.2) in two Frobenius series about the two singular points $z = \pm 1$ and match the solutions at an intermediate point, $z = 0$. The Frobenius series themselves are made continuous there by choosing the appropriate scaling. For fixed k we then search for the values of C at which the first derivatives of the two Frobenius series are also continuous across $z = 0$. The second derivatives are continuous, since both series satisfy (2.2).

Specifically, we write the solution near $z = +1$ as

$$\phi_+(z) = \sum a_m(1 - z)^{m+\alpha}. \tag{2.4a}$$

Substitution of Eq. (2.4a) into Eq. (2.2) yields the indicial equation $\alpha^2 = 0$, i.e. the regular solution at $z = 1$ has a simple Taylor series expansion. The coefficients $\{a_m\}$ satisfy the three-term recursion relation

$$a_0 = 1, \tag{2.4b}$$

$$a_1 = -a_0(k^2/4)(1 + 2C)^2, \tag{2.4c}$$

$$a_2 = a_0[k^2(3 + 4c)/2]/8 - a_1[2 - k^2(1 + 2C)^2/2]/8, \tag{2.4d}$$

$$\vdots$$

$$a_{m+1} = \{a_m[m(m + 1) - k^2(i + 2C)^2/2] + a_{m-1}k^2(3 + 4C)/2 - a_{m-2}3k^2/4\}/2(m + 1)^2, \quad m \geq 2. \tag{2.4e}$$

Near $z = -1$, the solution is

$$\phi_- = \sum b_m(1 + z)^{m+\beta}, \tag{2.5a}$$

with indicial equation $\beta^2 = 0$. The recursion relation for the coefficients $\{b_m\}$ is

$$b_0 = 1, \tag{2.5b}$$

$$b_1 = -b_0(k^2/4)(1 - 2C)^2, \tag{2.5c}$$

$$b_2 = b_0[k^2(3 - 4C)/2]/8 + b_1[2 - k^2(1 - 2C)^2/2]/8, \tag{2.5d}$$

$$\vdots$$

$$b_{m+1} = \{b_m[m(m + 1) - k^2(1 - 2C)^2/2] + b_{m-1}k^2(3 - 4C)/2 - b_{m-2}3k^2/4\}/2(m + 1)^2, \quad m \geq 2. \tag{2.5e}$$

According to (2.4b, 2.5b), the two series are normalized so that $\phi_\pm(\pm 1) = 1$. Their radius of convergence equals 2, so that at $z = 0$ both ϕ_+ and ϕ_- converge as $(1/2)^m + O(k^2/m^2)$. In practice, O(100) terms in the Frobenius series are sufficient to evaluate the functions and their derivatives at $z = 0$ accurately enough even for the largest values of k considered. Numerical experiments with a larger number of terms confirmed this estimate. In order to ensure that the functions and their first derivatives are continuous at $z = 0$, their logarithmic derivatives must be equal on both sides of $z = 0$. This translates into the following condition on C for arbitrary k:

$$\theta(k, C) \equiv (\sum a_m)(\sum mb_m) + (\sum b_m)(\sum ma_m) = 0; \tag{2.6}$$

here each of the Frobenius coefficients a_m and b_m depends on k and C through the recursion relations (2.4), (2.5).

For fixed k we have to find now the zero of the complex function $\theta \equiv \mathrm{Re}(\theta) + \mathrm{Im}(\theta)$ which depends on $C \equiv C_r + iC_i$. These zeros are found as follows. We first choose a range of C_i and a range of C_r, $C_i' < C_i < C_i''$ and $C_r' < C_r < C_r''$. Each range is divided into six equal intervals and the values of $\mathrm{Re}(\theta)$ and $\mathrm{Im}(\theta)$ are calculated at the 6×6 midpoints (j, l) of these intervals. The two matrices thus obtained, $\mathcal{R}_{jl} \equiv \mathrm{Re}(\theta(C_r^{(j)}, C_i^{(l)}))$ and $\mathcal{I}_{jl} \equiv \mathrm{Im}(\theta(C_r^{(j)}, C_i^{(l)}))$ are printed and we draw, in each matrix, the zero-crossing line(s), i.e. the line(s) along which the functions $\mathrm{Re}(\theta_{jl})$ and $\mathrm{Im}(\theta_{jl})$ change sign. In the next step we narrow the ranges of C_r and C_i by zooming into a region in (C_r, C_i)-space where a zero-crossing line in the $\mathrm{Re}(\theta)$ matrix intersects a zero-crossing line in the $\mathrm{Im}(\theta)$ matrix.

The procedure is repeated until the value of both functions is less than 10^{-5}, while the zero-crossing lines in the two matrices intersect each other. In some cases, lines which appear to cross each other on a coarse scale turn out to be parallel on a finer scale; in such cases the search for a zero of θ is stopped. This procedure is a variant on bisection algorithms (Isaacson and Keller 1966), and the choice of six, rather than two or a larger number of subintervals, is a matter of computational expediency, dictated by experience. Still, the algorithm is laborious, but detects *all* the zeros of θ in any subrange of (C_r, C_i), and no initial guess is required.

b. *Numerical results and analytical bound*

The dispersion relation $C_i = C_i(k)$ and the growth-rate curve—kC_i versus k—are shown in Figs. 2a and 2b. The real eigenvalues of the Legendre equation (2.3) are also indicated for small k in Fig. 2a. These analytical values agree very well with the numerical values for the real modes obtained by our zero finder. The unstable GKS mode, emanating from the origin ($k = 0$,

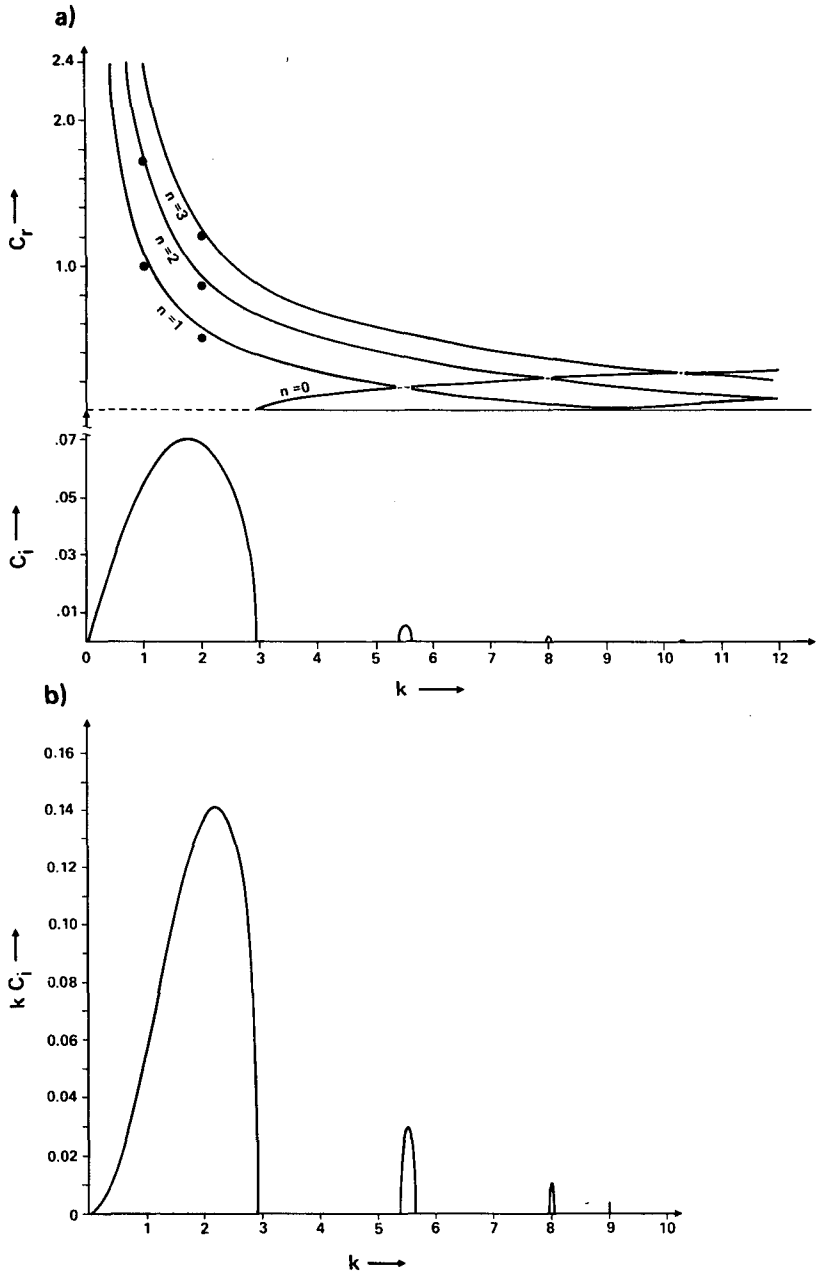

FIG. 2. The single-layer problem. (a) The real phase speeds and the instability exponents. Dots indicate real eigenvalues derived from Eq. (2.3). Instabilities appear in the dashed regions where two real phase speeds coalesce. The width of the coalescence regions diminishes with increasing wavenumber and so does the size of the instabilities. (b) The growth rate associated with the single-layer instabilities. Note that the instability exponents decay fast enough for the growth rate to decrease with wavenumber.

$C_i = 0$), is recalculated using the procedure described above. The values of $C_i(k)$ obtained here for this mode agree perfectly with those of GKS and PK.

In addition to the real and the GKS long-wave modes, our zero-finding procedure yields instabilities for finite values of k, with several noteworthy features. First, finite-wavelength instabilities are encountered whenever either the real phase speeds of two modes coalesce, $C_r(k; n_1) = C_r(k; n_2)$, or the phase speed of a certain mode vanishes, $C_r(k; n) = 0$. Second, as k increases, both C_i (Fig. 2a) and the growth rate kC_i (Fig. 2b) decrease. Thus the GKS mode is the most unstable one and other instabilities exist, but become negligible as k becomes large.

An analytical bound on all single-layer instabilities is obtained by letting both C and u in Eq. (2.2) be complex, multiplying by u^* (the complex conjugate of u) and integrating the resulting equation between $z = -1$ and $z = 1$ by parts. The imaginary and real parts of the resulting integrals are, respectively,

$$\frac{k^2}{4} \cdot 8iC_i \int_{-1}^{1} |u|^2(z - 2C_r)dz = 0, \quad (2.7a)$$

$$-\int_{-1}^{1} (1 - z^2)|u_z|^2 + \frac{k^2}{4}\int_{-1}^{1} |u|^2[3z^2 - 1 - 8zC_r + 8(C_r^2 - C_i^2)]dz = 0. \quad (2.7b)$$

Equation (2.7a) implies that, for $C_i \neq 0$,

$$2C_r \int_{-1}^{1} |u|^2 dz = \int_{-1}^{1} z|u|^2 dz, \quad (2.8)$$

i.e., $|C_r| \leqslant \frac{1}{2}$.

Substituting Eq. (2.8) back into Eq. (2.7b) and rearranging we get

$$\frac{4}{k^2}\int_{-1}^{1} (1 - z^2)|u_z|^2 dz = \int_{-1}^{1} |u|^2(3z^2 - 1 - 8|C|^2)dz, \quad (2.9)$$

where $|C|^2 \equiv C_r^2 + C_i^2$ has to satisfy

$$8|C|^2 \int_{-1}^{1} |u|^2 dz = \int_{-1}^{1} |u|^2(3z^2 - 1)dz - \frac{4}{k^2}\int_{-1}^{1} (1 - z^2)|u_z|^2 dz.$$

If u is normalized by $\int_1^1 |u|^2 dz = 1$, Eq. (2.8) yields

$$C_r^2 = \frac{1}{4}\left[\int_{-1}^{1} z|u|\,dz\right]^2$$

and (2.9) then implies

$$8C_i^2 = 3\int_{-1}^{1} z^2|u|^2 dz - 1 - 2\left[\int_{-1}^{1} z|u|^2 dz\right]^2 - \frac{4}{k^2}\int_{-1}^{1} (1 - z^2)|u_z|^2 dz. \quad (2.10)$$

The last two terms on the right-hand side (rhs) of (2.10) are nonpositive semi-definite, yielding the bound

$$8C_i^2 \leqslant 3\int_{-1}^{1} z^2|u|^2 dz - 1 \leqslant 3\int_{-1}^{1} z^2 dz \int_{-1}^{1} |u|^2 dz - 1 = 3\left[\frac{2}{3}\cdot 1\right] - 1 = 1$$

or

$$|C_i| \leqslant \frac{1}{2\sqrt{2}} \approx 0.35. \quad (2.11)$$

For an eigenfunction u with well-defined symmetry, i.e.

$$u(-z) = \pm u(z),$$

$z|u|^2$ is antisymmetric, and $C_r = 0$. This will lead to values of C_i closer to the bound (2.11). The maximum value encountered in Fig. 2a occurs indeed for $C_r(n = 0) = 0$, but the actual value of C_i is about one fifth of the bound calculated in (2.11), indicating that the last term on the rhs of (2.10) is not negligible.

We turn now to the two-layer problem, where the new finite-wavelength instabilities found in this section appear as the asymptotic limits of two-layer, continuous instabilities when the lower layer becomes infinitely deep.

3. The two-layer problem

a. Numerical results

The two-layer problem corresponds to finite depth ratio r in Fig. 1. The complete formulation for arbitrary upper-layer potential vorticity was given in PK. The nondimensional eigenvalue system can be written as

$$C[(r - H)p_y]_y = C(k^2C^2 - 1)h + k^2C(r - H)p - Up, \quad (3.1)$$

$$(U - C)u + (1 - U_y)v + \phi = 0, \quad (3.2)$$

$$k^2(U - C)v + u + \phi_y = 0, \quad (3.3)$$

$$hu - (hv)_y + (U - C)h = 0. \quad (3.4)$$

Here $H(y)$, $U(y)$, C and k are the same as in section 2, h is the perturbation depth of the upper layer, u is the downstream perturbation velocity of the upper layer, v is the cross-stream perturbation velocity multiplied by i/k ($i \equiv \sqrt{-1}$), and p is the lower-layer pressure, which is related to the upper-layer pressure ϕ by the hydrostatic relation $\phi = p + h$. The depth ratio, r, appears now explicitly in the equations.

Equation (3.1) is the lower-layer equation obtained when the two horizontal velocity components are eliminated in favor of the pressure. Equations (3.2), (3.3) are the x and y momentum equations in the upper layer, respectively, while Eq. (3.4) is the continuity equation for that layer. The boundary condition for the lower layer is that p decay away from the two free streamlines, by a proper choice, different for $y > 1$ and for $y < 0$, of the solution to the equation $p_{yy} = k^2p$, which is valid in the absence of the upper layer [see PK, Eqs. (2.7), (2.8)]. For the upper layer we require only that the solutions be well behaved on the free streamlines.

In the special case when the potential vorticity is zero in the upper layer, i.e., $U_y = 1$, we can eliminate v, h and ϕ to get the pair of equations for u and p

$$C[(r-H)p_y]_y = -C(k^2C^2-1)(U-C)u - [C(k^2C^2-1) - k^2C(r-H) + U]p, \quad (3.5)$$

$$(Hu_y)_y = k^2[H-(U-C)^2]u - k^2(U-C)p. \quad (3.6)$$

Equations (3.5), (3.6) possess badly-behaved solutions near the fronts and have, therefore, to be integrated away from the fronts.

We first symmetrize these equations in the same way Eq. (2.1) was transformed into Eq. (2.2). The iterative search for eigenvalues begins by guessing C for fixed k and r and making two integrations from the front $z = +1$ to the midpoint $z = 0$: one integration with $p = 0$, $u = 1$ at $z = +1$, and the second with $p = 1$, $u = 0$ there. Two more integrations are carried out from the other front, $z = -1$, to $z = 0$ with analogous initial data. The solution is then taken to be a linear combination of these four trial solutions. Choosing the amplitude of p at $z = -1$ to equal 1, we determine the three other constants by requiring that the jumps in u, p and u_z vanish at $z = 0$. The remaining jump, p_z, is now adjusted to zero by varying the guess for the phase speed, C, using a zero-finding algorithm. Alternatively one can find the eigenvalues, but not the eigenfunctions, by requiring that the determinant of the 4×4 matrix containing the values of u, p, $\partial u/\partial z$, $\partial p/\partial z$ at $z = 0$ from the four runs vanish. The difference between the two determinations of the eigenvalues was always insignificant, within the accuracy of Figs. 3 and 4.

We consider the eigenvalues first. Starting from arbitrary k and large r, we take as an initial guess for C the value found in section 2. Both k and r are then varied at each step, using as an initial guess the value of C obtained for nearby values of k and r. The result is the dispersion curve, $C_i(k)$, shown in the top and bottom panel of Fig. 3 for $r = 0.25$ and $r = 1.0$, respectively. These values of r correspond to the lower layer being 2 and 8 times deeper than the maximum upper layer's nondimensional depth of 0.125. The real phase speeds C_r obtained include only slight modifications of the branches of single-layer phase speeds derived in section 2. Hence, at these values of r, the instabilities are essentially those of the single-layer problem.

Additional modes, neutral as well as unstable, appear only when the lower layer becomes shallower ("thinner") than the upper layer. We consider small r-values since we shall be interested in coastal fronts as well (see §4), where the total depth is small and the lower layer is expected to be thin. In Fig. 4a we show the real and imaginary parts of C for $r = 0.15$, i.e., when the minimum lower layer's thickness is only a fifth of the maximum upper layer's depth. The growth rates, kC_i, associated with the instabilities of Fig. 4a are given in Fig. 4b. Comparing Figs. 2 and 4 we notice that additional real phase speeds exist for long waves (small k). It is these long-wave neutral modes, related in an essential way to the presence of a thin lower layer, that coalesce at higher wavenumbers to yield the vigorous short-wave instabilities encountered in Fig. 4.

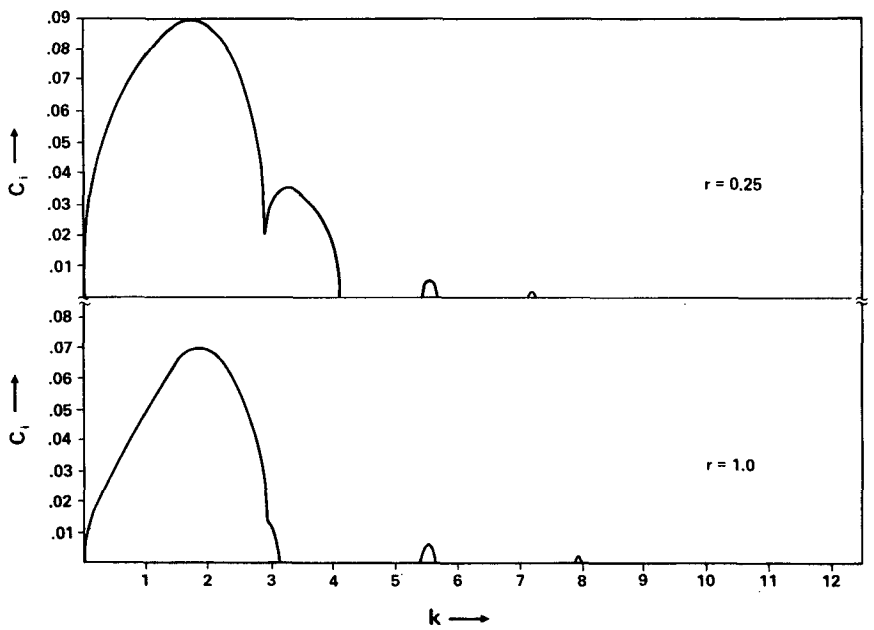

FIG. 3. Instability curves for the two-layer problem when the lower layer is deeper than the upper layer. Upper panel $r = 0.25$, lower panel $r = 1.0$. Note that the short-wave instabilities do not grow, and some even decrease, with decreasing r, whereas the long-wave instabilities grow with decreasing r.

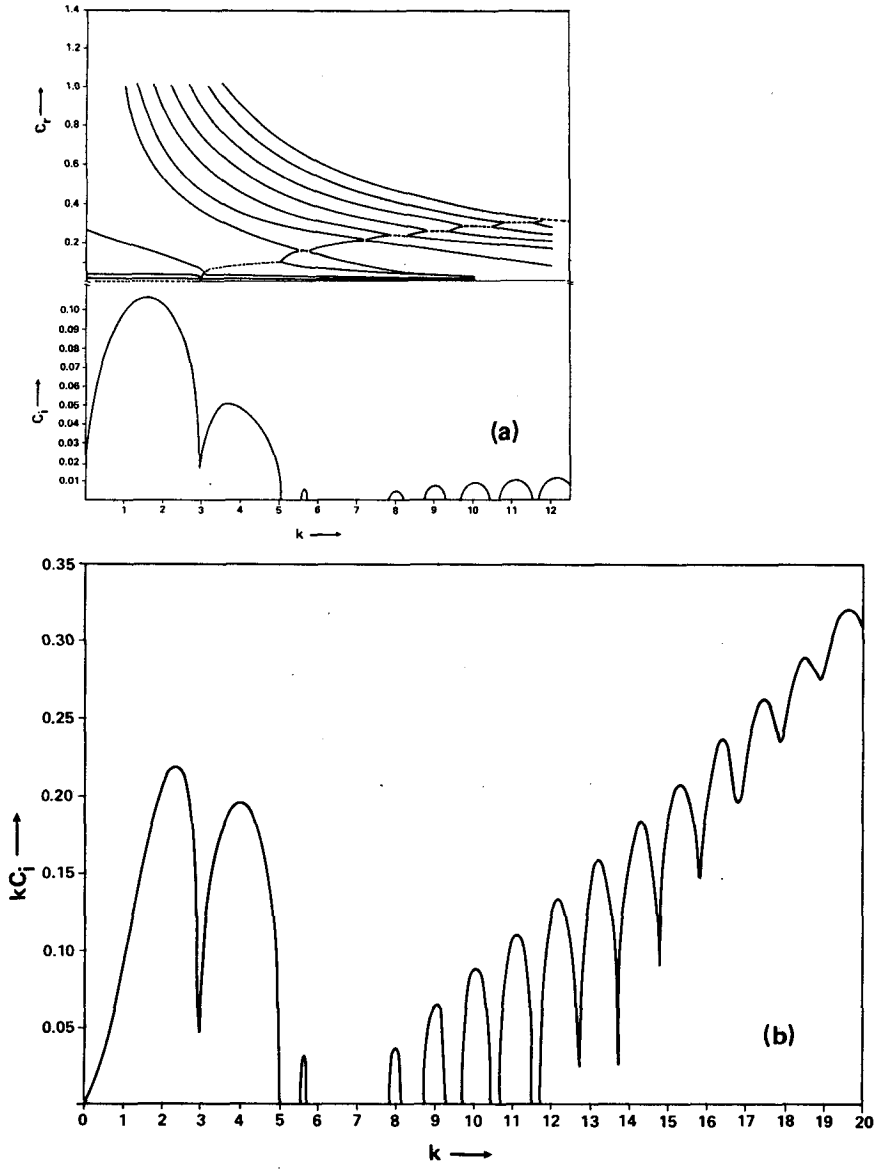

FIG. 4. As in Fig. 2, but for a shallow lower layer, $r = 0.15$. (a) C_r (upper panel) and C_i (lower panel); (b) growth-rate, kC_i. The separate coalescence regions merge into a continuous region beyond $k = 12$.

The dependence of these finite-wavelength instabilities on the depth ratio r, is shown in Fig. 5 for $k = 20$. For $r \leqslant 0.125$ the problem is not defined. For r-values above 0.2, i.e., when the two layers combined are only about 50% deeper than the upper layer's maximum depth, the short-wave instabilities vanish.

In addition to the continuation method, proceeding from large to moderate and small r, we also used the self-starting zero finder described in section 2. No additional instabilities were found.

The eigenfunctions of the homogeneous problem (3.5, 3.6) exhibit the well-known boundary-layer behavior associated with singularities at the two end points. From Eqs. (3.5), (3.6) it is clear that the u-components do have such singular end-point behavior, since $H \to 0$ at $z = \pm 1$, while the p-components do not. These observations are illustrated in Fig. 6. The real and imaginary parts of the eigenfunction in u are exponentially-large near the free streamlines, while the p-eigenfunction is regular there. The eigenfunctions illustrated in Fig. 6 are for $k = 10$ (see Fig. 4) and are typical of intermediate and large wavenumbers.

The symmetry associated with Legendre polynomials and present to a good approximation for large r and small k, cf. Eqs. (2.2), (2.3), is lost here. But each eigenfunction having larger amplitude along one free

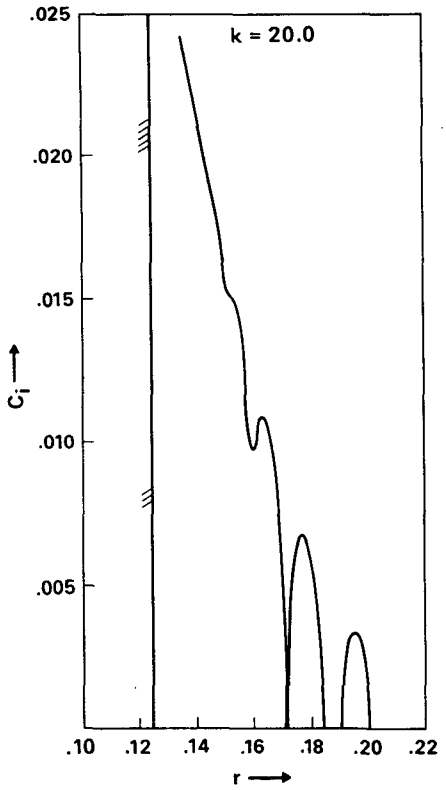

FIG. 5. The dependence of the instability exponent C_i on the depth ratio, r, for $k = 20$. The instability vanishes when r is above 0.2.

streamline has a mirror image associated with real phase speed C_r of opposite sign. The eigenfunctions illustrated in Fig. 6 are for positive C_r, i.e., phase propagation into the plane of the figure. The mirror-image eigenfunctions "living" near $z = -1$ propagate out of the plane of the figure.

b. *Analytical approximation*

The existence of additional long-wave neutral modes in the two-layer problem can be demonstrated analytically by considering their $k \to 0$ limit. In the single-layer problem, setting $k = 0$ in Eq. (2.2) yields only the trivial solution $u = 1$, with the eigenvalue C undetermined, although for small but finite k, neutral modes do obtain, cf. Eq. (2.3).

In the case of a shallow lower layer, nontrivial eigensolutions exist for infinitely-long waves, $k = 0$. To show this, we set $k = 0$ in the symmetrized version of Eqs. (3.5) and (3.6), with $z = 2y + 1$; let us call these symmetrical equations, analogous to (2.2), (3.5′), and (3.6′). For $k = 0$, Eq. (3.6′) yields the trivial solution $u \equiv u_0 = \text{const}$, while Eq. (3.5′) becomes

$$[(8r - 1 + z^2)p_z]_z - 2(z/C - 1)(p - Cu_0) = 0. \quad (3.7)$$

The frontal boundary conditions at $z = +1$ and $z = -1$ are $p_z = 0$.

Defining $\Phi = p - Cu_0$, Eq. (3.7) yields the following homogeneous equation for the function Φ

$$[(8r - 1 + z^2)\Phi_z]_z - 2(z/C - 1)\Phi = 0. \quad (3.8)$$

This equation cannot be easily solved for arbitrary r, but in the limiting case when $\delta \equiv 8r - 1 = 0$ a simple solution is obtained. This solution is of course accurate only to order δ, where $\delta = 0.2$ for $r = 0.15$. In the limit $\delta \to 0$, Eq. (3.8) becomes

$$[z^2\Phi_z]_z - 2(z/C - 1)\Phi = 0.$$

This has the simple solution

$$\Phi = z^{-1/2}J_3[(8z/C)^{1/2}],$$

where J_3 is the Bessel function of the first kind and order 3.

The first maximum of $J_3(y)/y$ occurs at $y \approx 4.5$ (Abramowitz and Stegun 1972, Table 9.2). This implies that the first, namely the highest, value of $\mathrm{Re}(C)$ is $C_r \approx 0.4$, a value which compares reasonably well (at order $\delta \approx 0.2$) with $C_r \approx 0.27$ at $k = 0$ in Fig. 4a.

c. *Energy conversions*

The energetics of the two-layer, coupled-front problem studied here parallels that of the two-layer, isolated-front problem studied by Killworth et al. (1984). The energy equation is obtained by multiplying the x and y momentum equations of the two layers by the corresponding velocity perturbation and unperturbed height, and the continuity equations of two layers by the perturbed heights (depths). Taking the x-average, denoted by angle brackets, and integrating with respect to y one gets:

$$\frac{d}{dt}\int E dy + \int_{-\infty}^{\infty} HU_y\langle uv\rangle dy + \int_{-\infty}^{\infty} U\langle \phi_x p\rangle dy = 0, \quad (3.9)$$

where u, ϕ, p, H and U are the same as in Eqs. (3.1)–(3.4) and v is the upper-layer velocity perturbation in the y direction, while E, the perturbation energy, is given by

$$E \equiv \left\langle H\left(\frac{1}{2}u^2 + \frac{1}{2}k^2v^2\right) + \frac{1}{2}h^2 + (r - H)\left(\frac{1}{2}u_2^2 + \frac{1}{2}k^2v_2^2\right)\right\rangle, \quad (3.10)$$

where u_2, v_2 are the velocity perturbations in the lower layer.

Equation (3.9) shows that the perturbation energy (3.10) can change either due to Reynolds stress in the upper layer or due to phase differences between upper and lower-layer pressure. Thus baroclinic energy con-

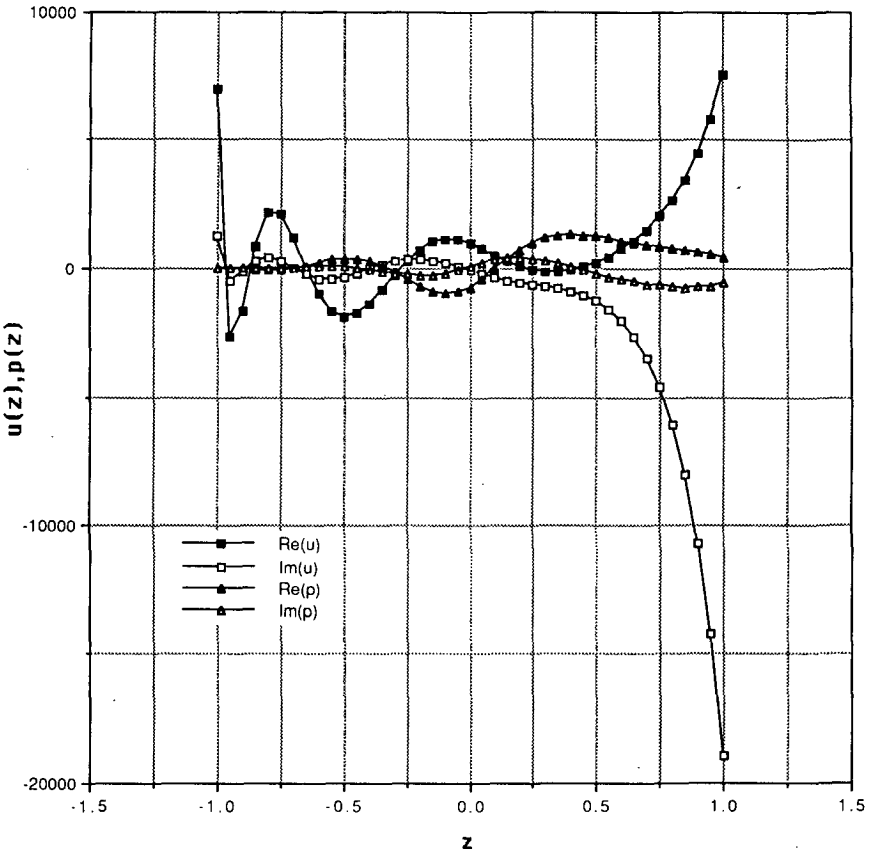

FIG. 6. The eigenfunctions $u(z)$ and $p(z)$ for $r = 0.15$ and $k = 10.0$. Eigenfunctions for higher values of r and other values of k are quite similar in appearance (not shown).

versions can fuel the vigorous short-wave instabilities, while the more-slowly growing, long-wave GKS instability had only barotropic energy conversion as an energy source.

4. Discussion and conclusions

The laboratory experiments described in GKS were all conducted in a system where the total depth is only between 1.1 and 8 times the upper layer's maximum depth. In almost all of their experiments, instabilities grow rapidly on a large range of spatial scales. The single-layer, long-wave theory of GKS fell short of explaining the observed results qualitatively, as well as quantitatively. The PK theory, which took into consideration the dynamics of the lower layer, could be adjusted to account quantitatively for some of the observed results. But the experimentally observed vigorous short-wave growth is beyond the range of applicability of the methods of PK, too, who merely extended long-wave results.

The theory presented in the preceding sections fills this gap by providing the growth rates of the short waves in both the single-layer and the two-layer problems. A marked difference between the two problems becomes apparent upon comparing Figs. 2 and 4. In the former, the short-wave instabilities diminish with increasing wavenumber and long waves dominate. In the latter case, where the minimum thickness of the lower layer is smaller than the maximum depth of the upper layer, the trend reverses and the short waves dominate, with a linearly increasing growth rate.

It is obvious that, at higher wavenumbers, some form of dissipation will become physically significant, and has to be included in the model. Dissipation will reverse, at sufficiently high k, the trend of the growth-rate curve by adding a term proportional to $-k^2$, and lead to the selection of a given short wave with maximum growth rate.

A quantitative comparison between the GKS experiments and our numerical results for the dependence of the growth rate on depth ratio r is impossible, as no direct measurement of the growth rate itself was reported by GKS. It is possible, however, to estimate visually the horizontal scale of the growing disturbances in the GKS experiments. In comparing the dependence of the selected wavelength with our results, we should

keep in mind that wider upper layers, as well as faster rotation rates, in the GKS experiments are both equivalent to a smaller r in our theory. This is due to the particular choice of depth scale H (Fig. 1) such that the nondimensional width of the upper layer is always 1, while the nondimensional interface depth is a parabola of height ⅛. H is thus proportional to the width squared and to f^2, where f is the Coriolis parameter.

Let us compare therefore the dominant wavelengths in the GKS experiments with different upper layer widths and different rotation rates (their Figs. 9, 10, 11 and 12). From the pair of experiments shown in Figs. 9 and 10, as well as from the pair of Figs. 11 and 12, it is readily apparent that smaller r-values lead to much smaller scales dominating the growth of the perturbation. This qualitative observation is in excellent agreement with the main results of our one- and two-layer calculations.

In addition to the laboratory experiments of GKS, there are numerous observations on the growth of perturbations along coastal fronts. A coastal front involves a relatively rapid transition between upwelled cold waters and warmer surface waters. The rapid-transition region can be approximated, as for isolated or coupled fronts, by an interface. In the case of the coastal front, this interface intersects the coast at some depth.

A coastal front studied intensively in recent years is the California Current front, which forms along the U.S. West Coast when cold, deep water upwells and starts flowing perpendicular to the temperature gradient because of geostrophy. It has long been observed that, along the free streamline of this front, vigorously-growing perturbations develop, which appear in satellite sea-surface temperature images as narrow and long tongues of cold water extending seaward. The along-coast width of these tongues is quite small, while their cross-coast amplitude is very large (Flament et al. 1985). Similar observations were reported by Arnone and LaViolette (1986) along the Mediterranean coast of North Africa, and by Ikeda et al. (1984) off Vancouver Island.

The presence of such vigorously-growing short-wave perturbations on coastal fronts can be related to our theory in the case in which the coastal current has a vanishing mean downstream velocity right at the coast. In this case, the symmetric problem encountered when placing a vertical wall in the middle of the front shown in Fig. 1 is very similar to the coastal-front problem. It is necessary to explore the cases in which the angle between the frontal interface and the coast, in a cross-coast vertical plane, is both larger and smaller than 90°. But the present work suggests that the technique used here will permit us to study short-wave instabilities on coastal fronts as well.

To summarize,

1) The long-wave instabilities found analytically by GKS, and explored further by PK, have the fastest growth rate in the single-layer problem.

2) The short-wave instabilities of the two-layer front reported in this work have the highest growth rate overall; this growth rate increases linearly with wavenumber provided the maximum depth of the upper layer exceeds half the depth of the two layers combined.

3) Baroclinic energy conversion helps fuel the rapid growth of the short-wave instabilities in the two-layer problem.

4) The growing perturbations are concentrated along the free streamlines, traveling within the lighter water to the right when looking from the heavier water, in the direction of the mean flow.

Acknowledgments. It is a pleasure to thank D. Deutsch, B. Gola, C. Monroe and C. Wong for help with the typing, and K. Martelli for help with the figures. The comments of one out of three referees were especially constructive and helpful. This research was supported by ONR Grants N00014-87-K0331, N00014-89-J1845 and by a UCAR grant administered by the Institute of Naval Oceanography.

REFERENCES

Abramowitz, M., and I. A. Stegun, 1972: *Handbook of Mathematical Functions.* Dover, 1046 pp.

Arnone, R. A., and P. E. LaViolette, 1986: Satellite definitions of the bio-optical variation of the coastal eddies associated with the African current. *J. Geophys. Res.*, **91,** 2351–2364.

Flament, P., L. Armi and L. Washburn, 1985: The evolving structure of an upwelling filament. *J. Geophys. Res.*, **90**(C6), 11 765–11 778.

Ghil, M., and S. Childress, 1987: *Topics in Geophysical Fluid Dynamics: Atmospheric Dynamics, Dynamo Theory and Climate Dynamics.* Springer-Verlag, 485 pp.

Griffiths, R., P. D. Killworth and M. E. Stern, 1982: Ageostrophic instability of ocean currents. *J. Fluid Mech.*, **117,** 343–371.

Ikeda, M. W., W. J. Emery and L. A. Mysak, 1984: Seasonal variability in meanders of the California current system off Vancouver Island. *J. Geophys. Res.*, **89,** 3487–3505.

Isaacson, E., and H. B. Keller, 1966: *Analysis of Numerical Methods.* Wiley and Sons, 541 pp.

Killworth, P. D., N. Paldor and M. E. Stern, 1984: Wave propagation and growth on a surface front in a two-layer geostrophic current. *J. Mar. Res.*, **42,** 761–785.

Paldor, N., 1986: Nonlinear waves on a coupled density front. *Geophys. Astrophys. Fluid Dyn.*, **37,** 171–191.

——, and P. D. Killworth, 1987: Instabilities of a two-layer coupled front. *Deep-Sea Res.*, **34**(a), 1525–1539.

Pedlosky, J., 1987: *Geophysical Fluid Dynamics,* 2nd ed. Springer-Verlag, 710 pp.

Smith, P. C., 1976: Baroclinic Instability in the Denmark Strait overflow. *J. Phys. Oceanogr.*, **6,** 355–371.

Whitehead, J. A., and L. V. Worthington, 1982: The flux and mixing rates of Antarctic Bottom Water within the North Atlantic. *J. Geophys. Res.*, **87,** 7903–7924.